Supporting information

Practical Zn anodes enabled by a Ti-MOF-derived coating for aqueous batteries

Qiuju Xu[a], Wencai Zhou[b], Tuo Xin[a], Zilong Zheng[b,], Xiangcheng Yuan[a], Jinzhang Liu[a,*]

[a] School of Materials Science and Engineering, Beihang University, Beijing, China

*E-mail: ljz78@buaa.edu.cn

[b] Department of Materials and Manufacturing, Beijing University of Technology, Beijing 100124, China

Experimental Section

Electropolymerization of poly(1,5-naphthalenediamine)

The polymer cathode was prepared by electrodepositing poly(1,5-naphthalenediamine) onto a coating of nanoporous activated carbon (AC). First, a slurry was made by dispersing AC power (YP-80, Kuraray Co.), carbon black, and polyvinylidene difluoride as binder at a weight ratio of 8:1:1 into N-methyl pyrrolidone. The slurry was coated onto a 3 mm-thick carbon fiber felt, followed by a drying process. The mass loading of AC coating is ~31 mg cm^{-2}. Second, the AC-coated carbon felt was used as work electrode in a three-electrode cell containing 1 M H_2SO_4 solution and 0.02 M 1,5-NAPD molecules. With a Pt foil as counter electrode and an Ag/AgCl reference electrode, the electropolymerization was conducted by running cyclic voltammogram (CV) cycles at 20 mV s^{-1} within the voltage range from – 0.4 to 1.0 V for 300 cycles. Third, the poly(1,5-NAPD)/AC was rinsed with deionized water and dried overnight.

Electrochemical measurements

An electrochemical workstation (CorrTest CS 310) was used in this experiment. The linear polarization was tested at a voltage sweep rate of 0.5 mV s^{-1} within the voltage range from – 1.08 to – 0.88 V. A Zn foil as counter electrode and an Ag/AgCl reference electrode were used, and the electrolyte was 3 M $ZnSO_4$ aqueous solution. The linear sweep voltammetry (LSV) was measured in a 3 M $ZnSO_4$ aqueous electrolyte at a voltage sweep rate of 0.1 mV s^{-1}. Hydrogen gas evolution would be occurred when the potential is below – 1.05 V. The cycling performance of the MnO_2-based full cells was measured by the battery test system (LAND CT3001A) in the voltage range of 0.9 – 1.9 V. Electrochemical impedance spectroscopy (EIS) of the cells were conducted on the electrochemical workstation over the frequency range 100 kHz – 0.01 Hz.

Density function theory simulation

All the calculations were performed with density function theory (DFT) as implemented in CP2K/*Quickstep* package,[1] while method D3 developed by Grimme et al.[2] includes the dispersion correction and adds van der Waals interaction to the conventional Kohn-

Sham potential energy. The function of the standard Perdew-Bueke-Ernzerhof (PBE) generalized gradient approximation (GGA),[3] was employed for exchange correction interactions, within the framework of Gaussian and plan wave (GPW) method.[4] The wave functions of the valence electrons were expanded in terms of Gaussian functions with molecularly optimized (MOLOPT) double ζ polarized basis sets (m-DZVP),[5] which ensures a small basis set superposition error (BSSE) in gas and condensed phase, and core electrons were described with norm-conserving Goedecker-Teter-Hutter (GTH) pseudopotentials.[6] The energy cutoff for the plane-wave was set at 500 Ry. All the atoms are allowed to relax until the force on each atom is less than 0.01 eV/Å.

Structural characterizations

Fig. S1 shows FESEM images of as-prepared Ti-MOF. Each Ti-MOF granule is regularly shaped, with width of ~ 800 nm and thickness of 400 nm. Fig. S2 shows a XRD pattern of the Ti-MOF product.

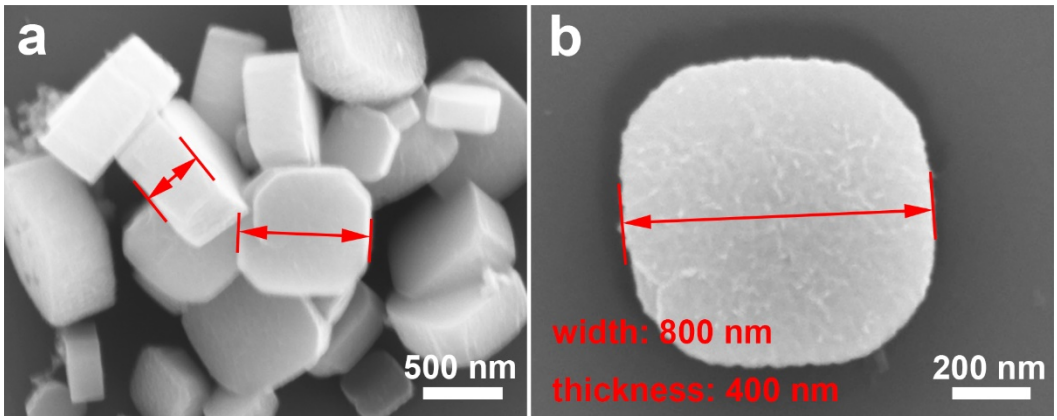

Fig. S1 (a) Low- and (b) high-magnification FESEM images of the Ti-MOF precursor.

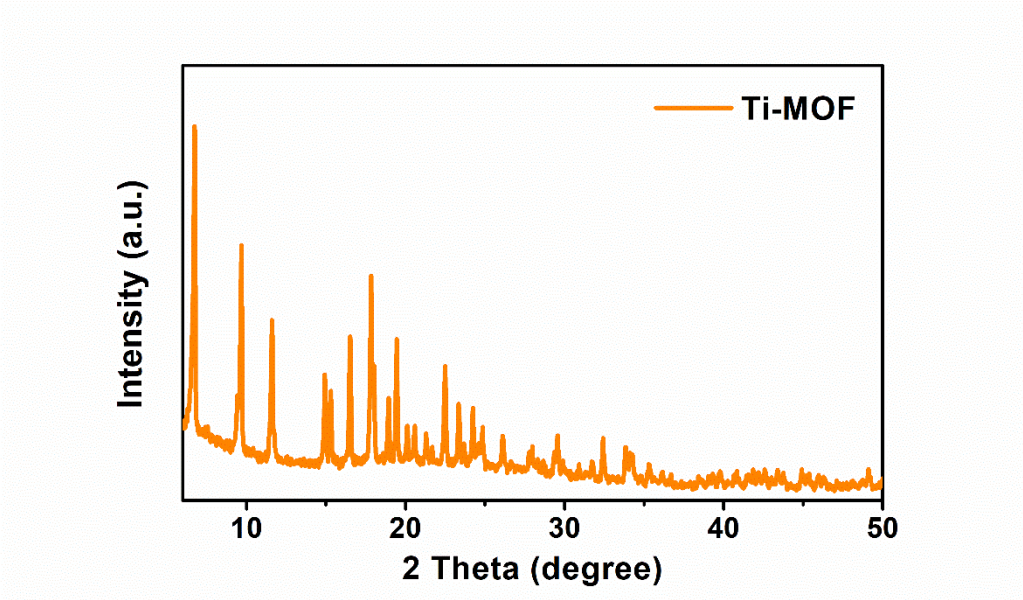

Fig. S2 XRD pattern of the Ti-MOF precursor.

The Ti-MOF was converted into TiO_2/NC after being calcined in Ar. A FESEM image of the TiO_2/NC granules is shown in Fig. S3a. Correspondingly, EDS elemental mappings for Ti, O, C, and N distributions over the TiO_2/NC granules are shown in Fig. S3b.

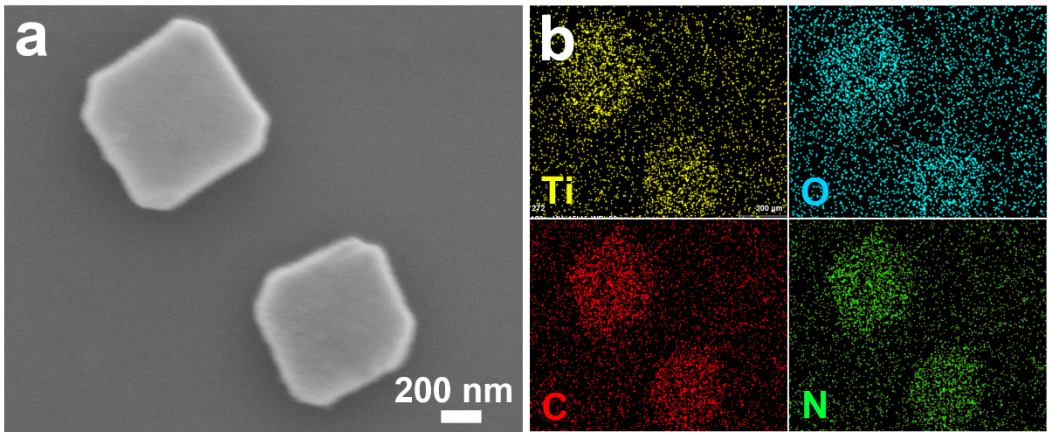

Fig. S3 (a) FESEM image and (b) corresponding element mappings of TiO_2@NC granules.

The TiO_2 sample was obtained by calcining Ti-MOF in air. Our XRD analysis confirms the anatase TiO_2, as shown in Fig. S4a. A FESEM image of this TiO_2 product is shown in Fig. S4b. Although the carbon was burned out, TiO_2 nanoparticles were inter-connected and the original shape of Ti-MOF was maintained. The NC product was also obtained by etching away TiO_2 in the TiO_2/NC product using HCl solution. The XRD pattern in Fig. S4c shows a broad peak of graphitic carbon, and no any peak from TiO_2. Also, the NC granules maintain the original cubic shaped of Ti-MOF, as shown in Fig. S4d.

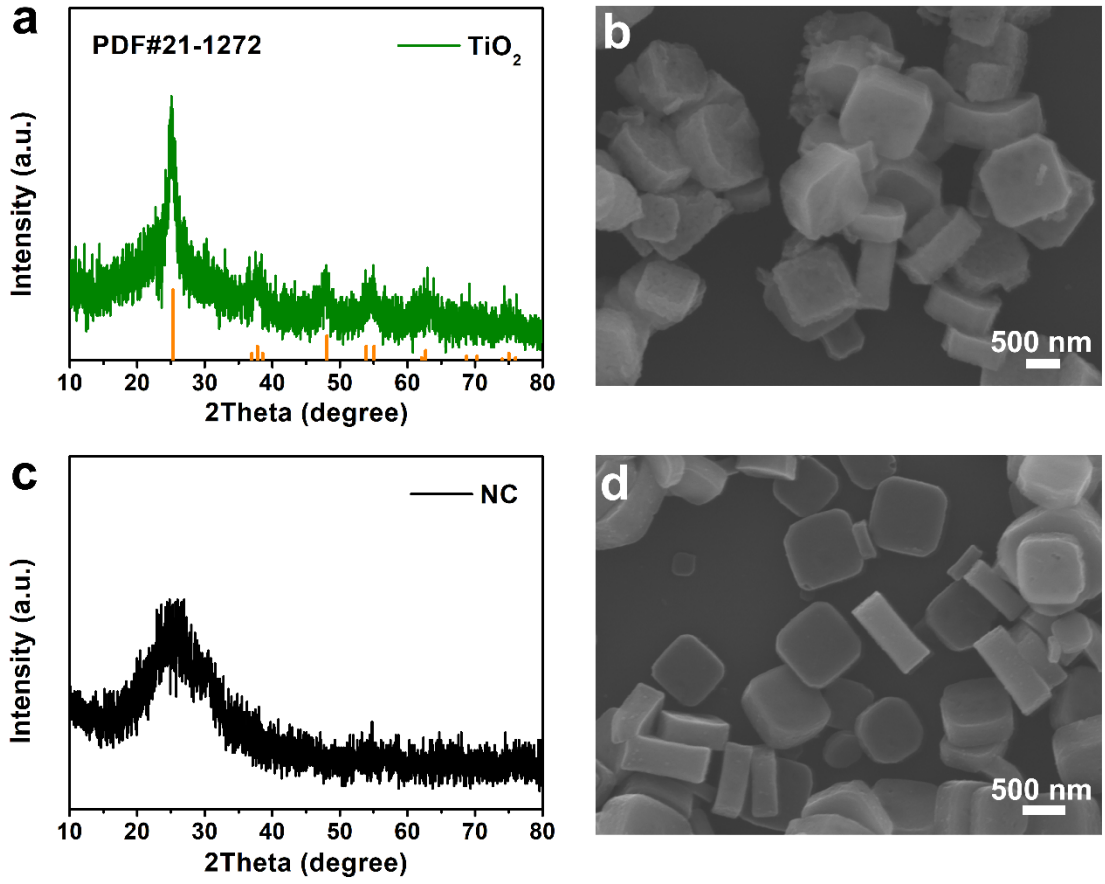

Fig. S4 (a) XRD pattern and (b) FESEM image of anatase TiO_2 derived from Ti-MOF. (c) XRD and (d) FESEM image of the NC product made by etching away TiO_2 in TiO_2/NC composite.

Fig. S5 shows a survey XPS spectrum of the TiO_2/NC product.

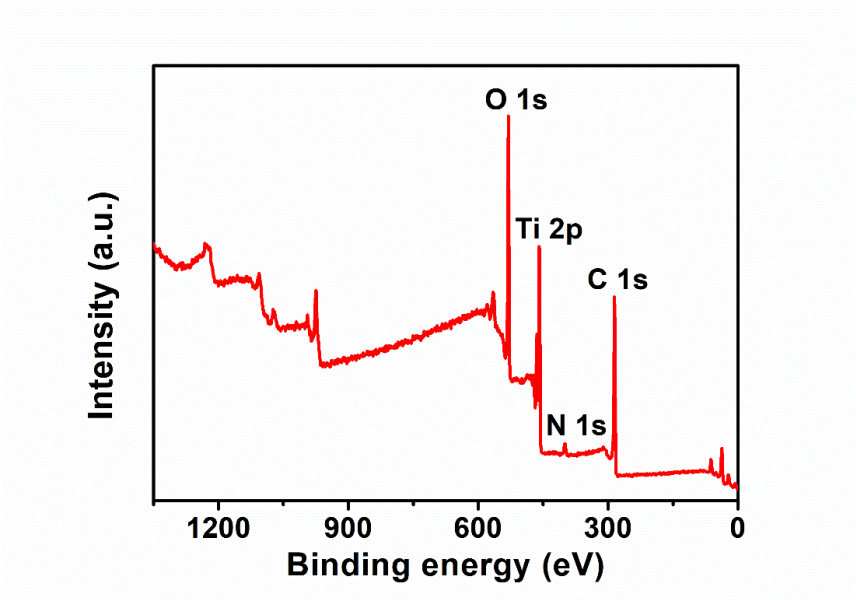

Fig. S5 Survey XPS spectrum of the TiO_2/NC composite.

BET measurement of the TiO_2/NC composite

Fig. S6 shows the BET measurement result of the TiO_2/NC samples. According to the N_2 adsorption-desorption isotherm in Fig. S6a, the specific surface area of TiO_2/NC composite is determined to be 138 m^2 g^{-1}. The pore size distribution of this this sample is shown in Fig. S6b.

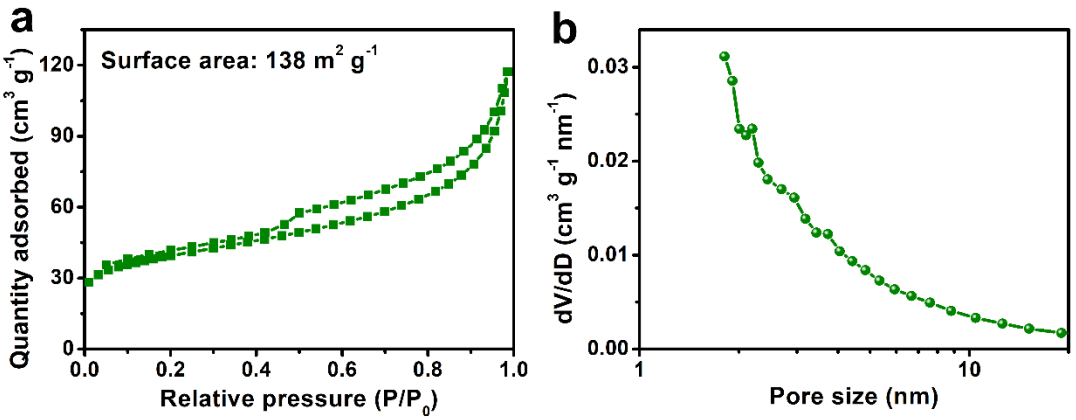

Fig. S6 BET measurement result of the TiO_2/NC product. (a) N_2 adsorption/desorption curves at room temperature. (b) BJH pore size distribution.

Wettability tests on NC and TiO_2/NC coatings

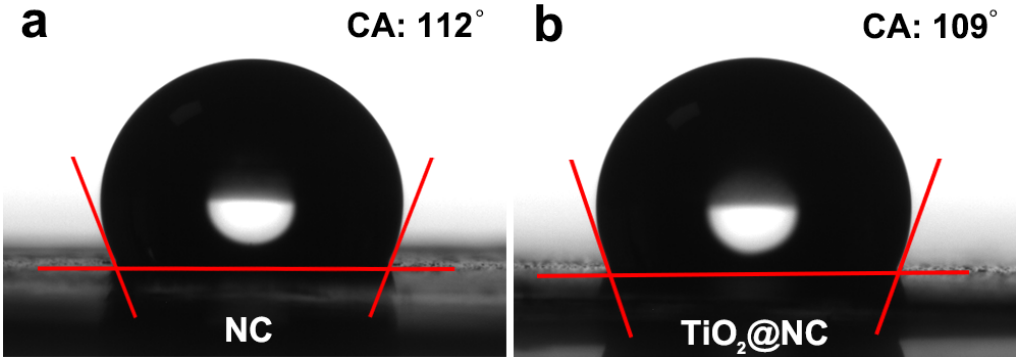

Fig. S7 Contact angle of (a) the NC coating and (b) the TiO_2/NC coating.

Anti-corrosion performance

A bare Zn foil and a Zn@TiO_2/NC disk were kept in two vials containing 3 M $ZnSO_4$ solution, respectively, as shown in Fig. S8a. After being immersed for one week, the originlly shiny Zn foil presented white color products due to corrosion, while the black Zn@TiO_2/NC remained unchanged in appearance, as shown in Fig. S8c. Our XRD analysis revealed that the byproduct over corroded bare Zn is $ZnSO_4(OH)_6$•xH_2O, and the Zn@TiO_2/NC sample after 1-week immersion in $ZnSO_4$ solution was almost free of this byproduct, as shown in Fig. S8b.

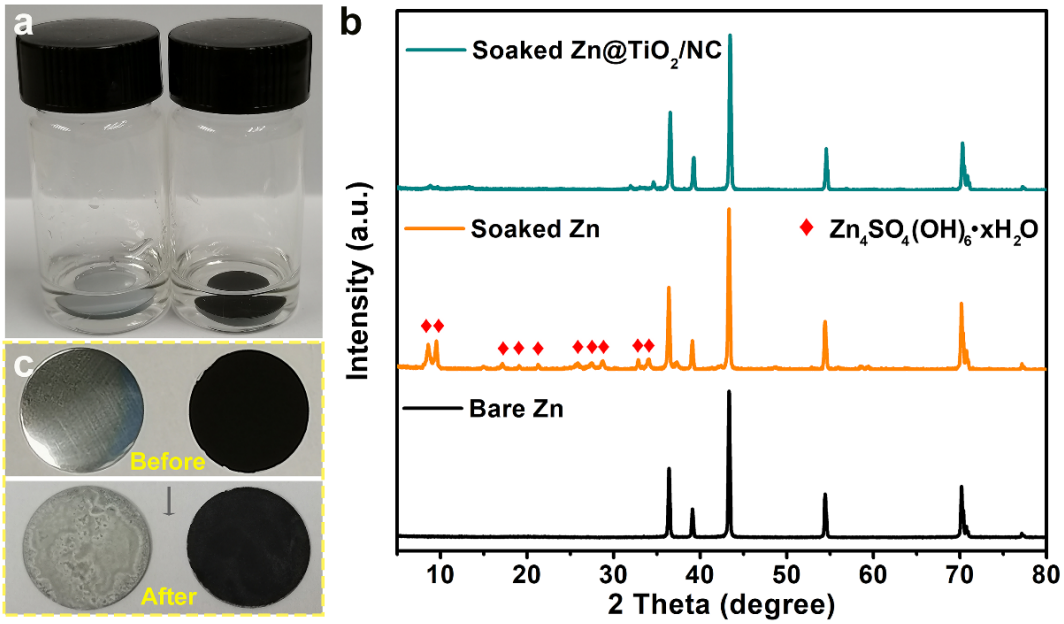

Fig. S8 (a) Optical photographs of a bare Zn disk and a Zn@TiO_2/NC disk immersed

in 3M $ZnSO_4$ electrolyte for 7 days. (b) XRD patterns of the bare Zn and the Zn@TiO_2/NC foil before and after the natural corrosion process in $ZnSO_4$. (c) Optical photographs of a bare Zn disk and a Zn@TiO_2/NC disk before and after the natural corrosion test.

Electrochemical tests

Two symmetric pouch cells using bare Zn and Zn@TiO_2/NC, respectively, were cycled at identical current density, and the results are shown in Fig. S9.

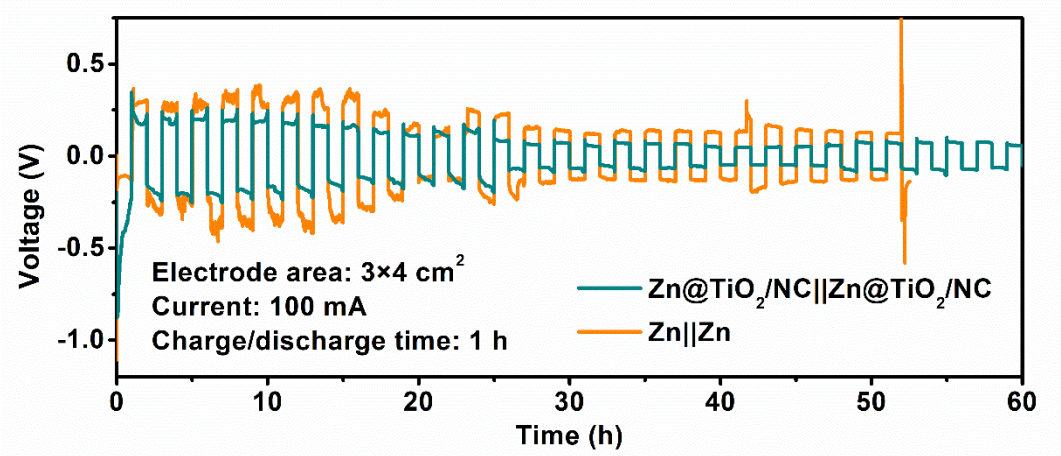

Fig. S9 Cycling performance of symmetric pouch cells using bare Zn and Zn@TiO_2/NC, respectively.

In order to demonstrate the efficacy of Zn@TiO_2/NC in suppressing hydrogen gas evolution, a high-capacity poly(1,5-NAPD)/AC cathode based on carbon fiber felt was made. The thickness of carbon fiber felt is 3 mm and the mass loading of poly(1,5-NAPD)/AC is over 30 mg cm^{-2}, which can provide a high areal capacity over 5 mAh cm^{-2}. Thus the opposite cathode can be stripped/plated at a high current and with large depth beyond 10 μm. Generally, the rate of H_2 generation is related to the areal current density of the anode. Hence, suppression of H_2 generation at a high charge-discharge

current is critical for a practical ZIB. In our experiment, a beaker-based full cell was used to observe the H_2 evolution over bare Zn or Zn@TiO_2/NC surfaces when charged/discharged at 20 mA cm^{-2}. As shown in Fig. S10a and b, with prolonging the cycling time, more and more bubbles were emerged over the bare Zn anode. However, for the Zn@TiO_2/NC anode, it was nearly free of bubbles after being cycled for 10 cycles (Fig. S10a). After 20 cycles, a few bubbles were emerged near the top edge of the anode, presumably the current near the electrolyte surface is higher.

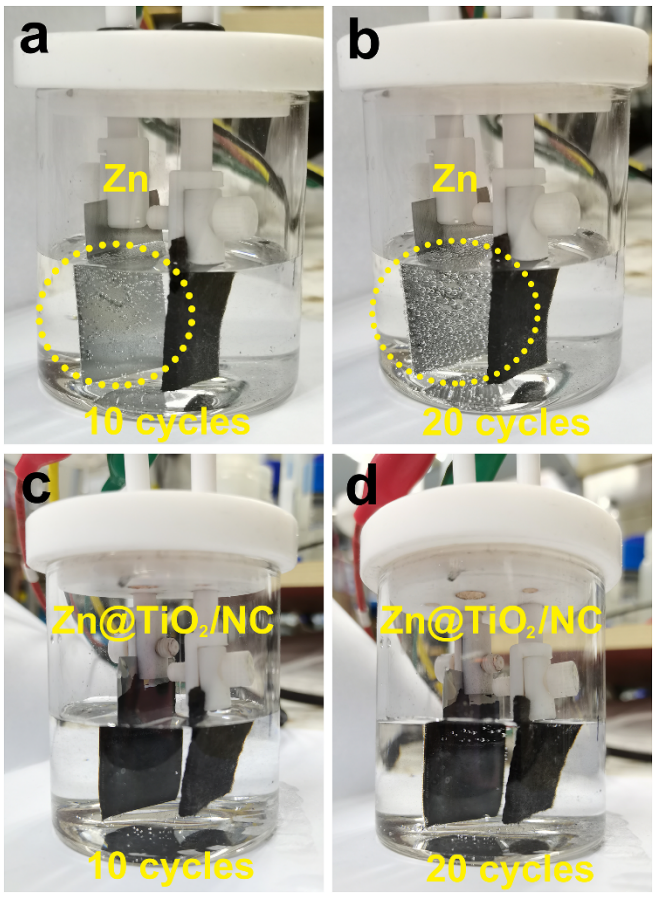

Fig. S10 Beaker-based full cells using a high-capacity poly(1,5-NAPD)/AC cathode to observe the H_2 evolution behaviors of the bare Zn and the Zn@TiO_2/NC by running charged/discharged cycles at 20 mA cm^{-2}.

Fig. S11 shows chronoamperometry (CA) curves of a bare Zn anode and a Zn@TiO_2/NC anode under constant voltage of - 210 mV.

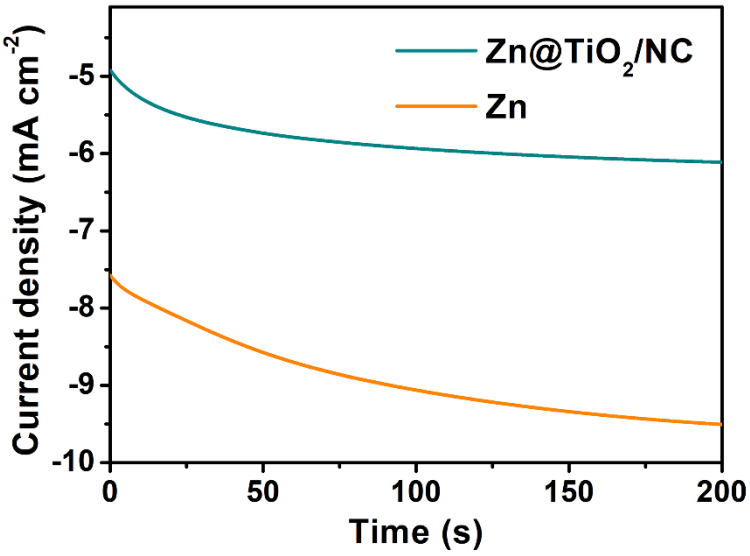

Fig. S11 Chronoamperometry (CA) curves of a Zn@TiO_2/NC anode and a bare Zn anode at constant potential of - 210 mV.

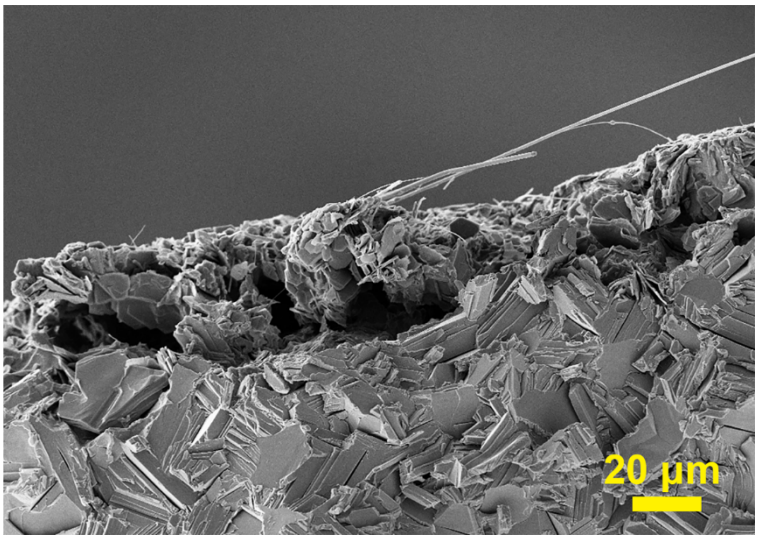

Fig. S12 Cross-sectional FESEM image of a cycled bare Zn anode.

Half cells using Zn@NC and Zn@TiO_2 anodes, respectively to match with Ti were cycled at 2 mA cm^{-2} with set capacity of 1 mAh cm^{-2}, and the results are shown in Fig.

S13. For other two half cells using Zn@TiO_2/NC and bare Zn anodes, respectively, their variations of Coulombic efficiency (CE) in the cycling process in shown in Fig. S14a. Also, voltage-capacity plots of the two cells tested at 5 mA cm^{-2} with set capacity of 1 mAh cm^{-2} are shown in Fig. S14b and c, respectively.

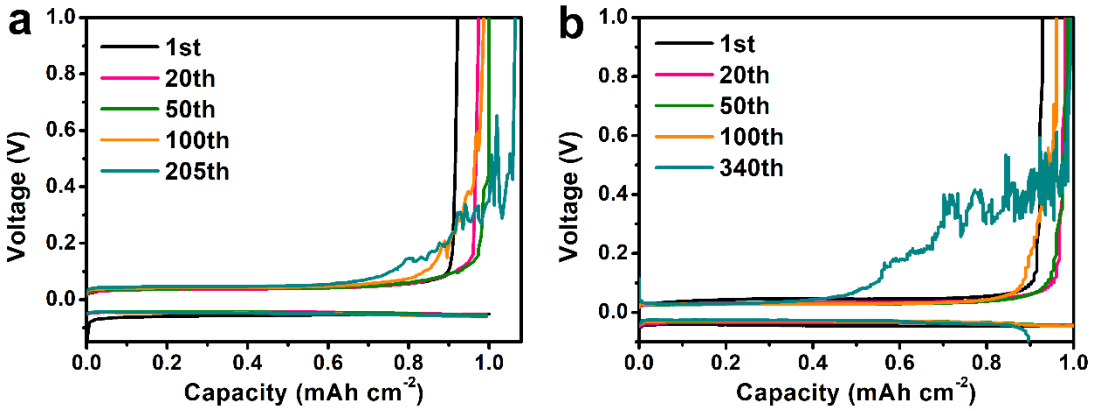

Fig. S13 Charge/discharge curves for (a) Ti||Zn@NC and (b) Ti||Zn@TiO_2 asymmetric cells at current density of 2 mA cm^{-2} and set capacity of 1 mAh cm^{-2}.

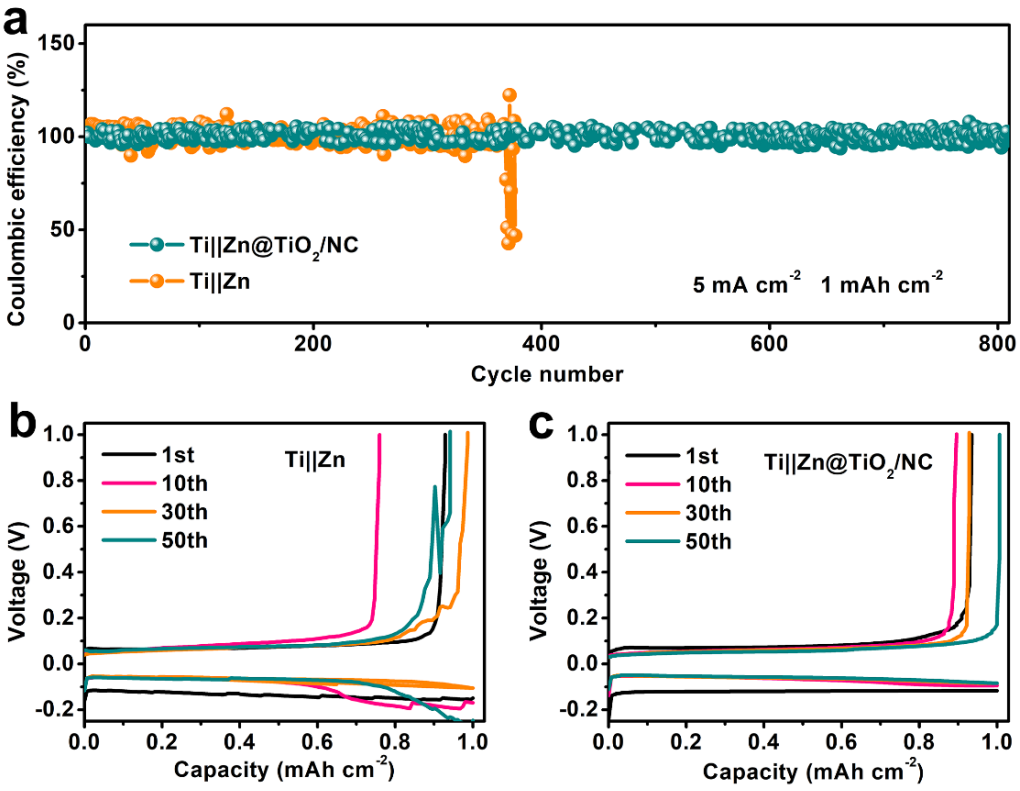

Fig. S14 (a) Variations of CE values of a Ti||Zn and a Ti||Zn@TiO_2/NC cell at current density of 5 mA cm^{-2} and set capacity of 1 mAh cm^{-2}. The charge/discharge curves of

(b) the Ti||Zn cell and (c) the Ti||Zn@TiO_2/NC cell after different cycles.

Fig. S15 shows room-temperature EIS spectra of three symmetric cells using bare Zn, Zn@TiO_2/NC, and Zn@TiO_2, respectively. The R_{ct} values of the three anodes are in the sequence of Zn@TiO_2/NC < Zn@TiO_2 < Zn.

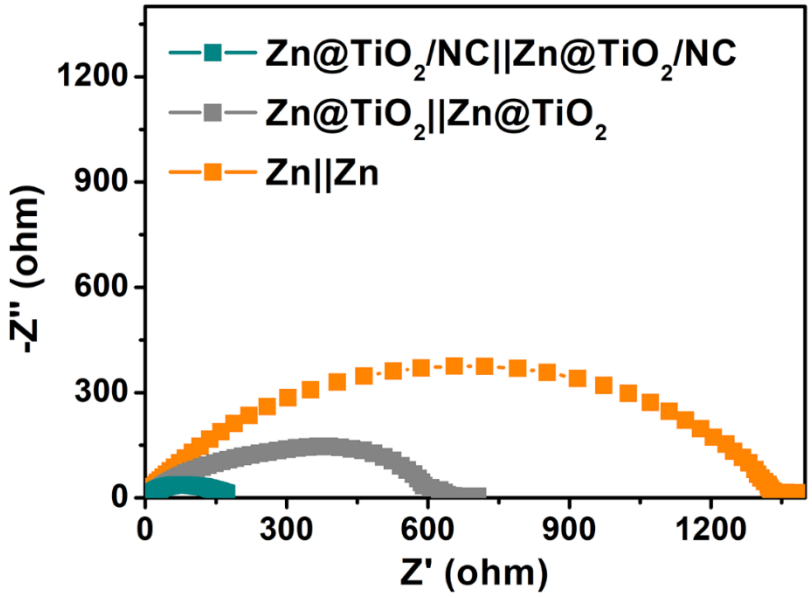

Fig. S15 Room-temperature Nyquist plots of symmetric cells using bare Zn, Zn@TiO_2 and Zn@TiO_2/NC anodes.

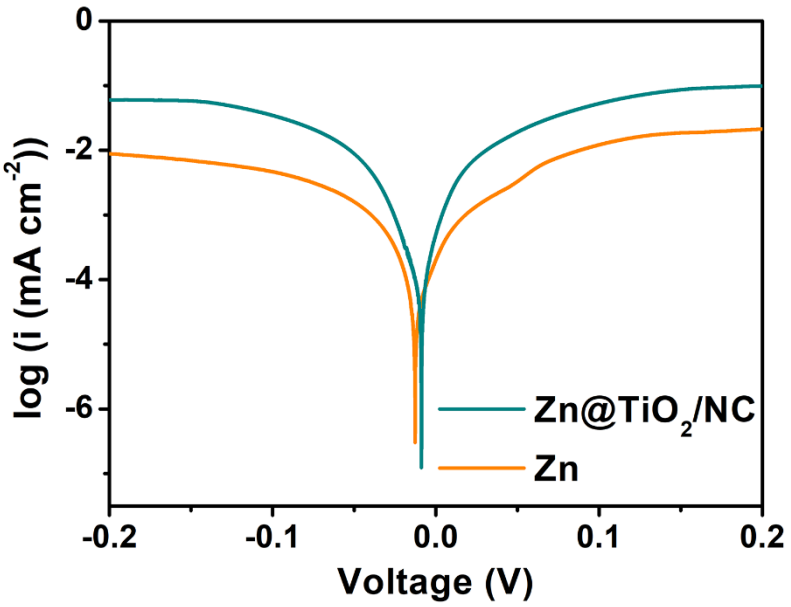

Fig. S16 Linear polarization curves of symmetric cells using Zn@TiO_2/NC and bare Zn, respectively.

The consequence of H_2 evolution could make the cell swell or even burst. Figure S17a and b show two symmetric cells using bare Zn and Zn@TiO_2/NC, respectively, after the cycling test.

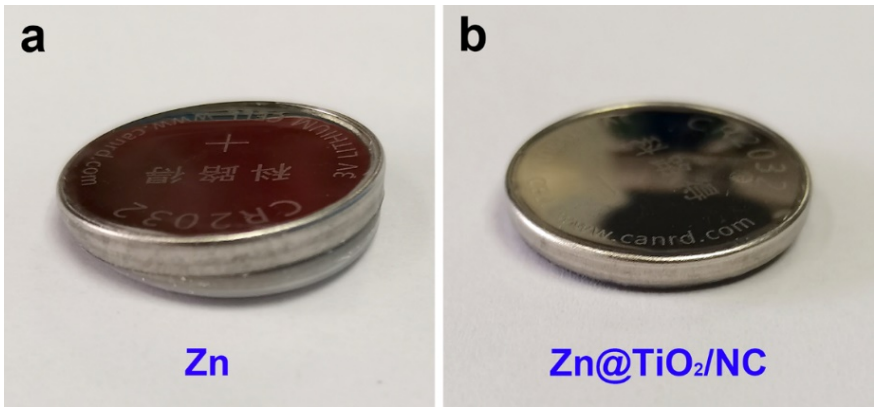

Fig. S17 Optical photographs of (a) a Zn||Zn and (b) a Zn@TiO_2/NC||Zn@TiO_2/NC symmetric cell after being cycled.

Symmetric cells using Zn@TiO_2/NC, Zn@TiO_2, and bare Zn were further tested by running charge-discharge cycles at different current densities and capacities. Cycling performances of the two symmetric cells using bare Zn and Zn@TiO_2/NC, respectively, tested at 0.5 mA cm^{-2} and 0.25 mAh cm^{-2}, are compared in Fig. S18. In Fig. S19, cycling stabilities of three cells using bare Zn, Zn@TiO_2, and Zn@TiO_2/NC, respectively, and tested at 2 mA cm^{-2} and 1 mAh cm^{-2}, were compared. For the cycling performances of cells tested at higher current, Fig. S20a shows the results of two cells using bare Zn and Zn@TiO_2/NC, respectively, tested at 10 mA cm^{-2} and 1 mAh cm^{-2}. From the practical point of view, a high capacity of ZIB cathode helps increasing volumetric energy density, thus the metal anode is also required to offer a high areal capacity in operation. Hence, we tested the symmetric cell using Zn@TiO_2/NC at 10 mA cm^{-2} and 5 mAh cm^{-2}, which means a fast charge/discharge rate and large depth of ~ 8.5 μm for Zn stripping/platting. As shown in Fig. S20b, the Zn@TiO_2/NC anode could sustain 200 cycles even operated at 10 mA cm^{-2} and 5 mAh cm^{-2}.

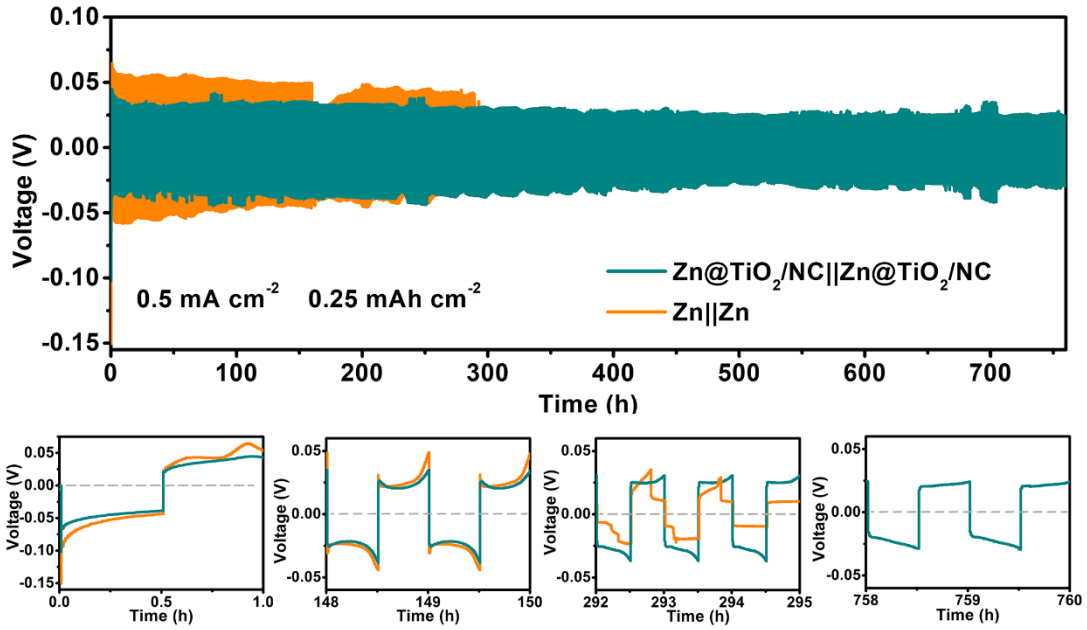

Fig. S18 Cycling performances of symmetric cells using bare Zn and Zn@TiO_2/NC, respectively, tested at 0.5 mA cm^{-2} and set capacity of 0.25 mAh cm^{-2}.

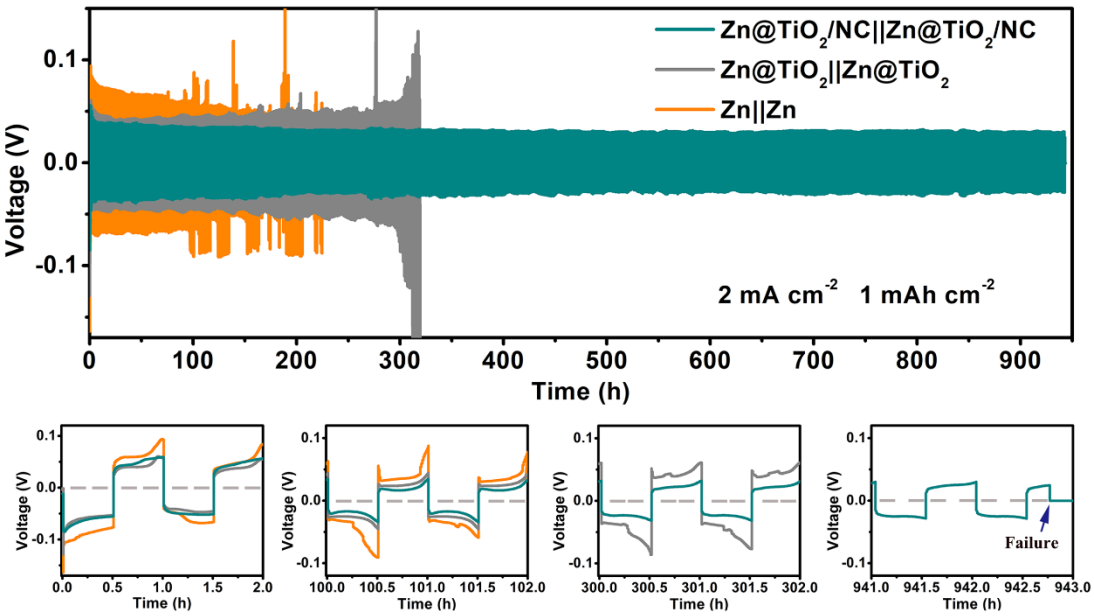

Fig. S19 Cycling performances of symmetric cells using bare Zn, Zn@TiO_2, and Zn@TiO_2/NC, respectively, tested at 2 mA cm^{-2} and set capacity of 1 mAh cm^{-2}.

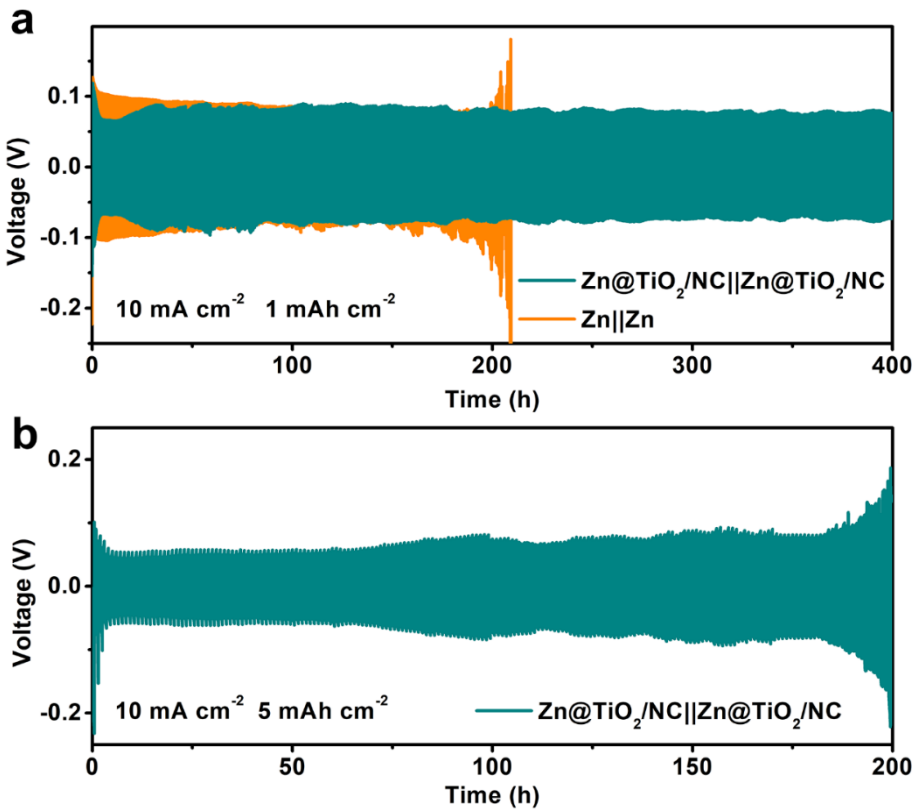

Fig. S20 Cycling performance of (a) Zn||Zn and Zn@TiO_2/NC||Zn@TiO_2/NC symmetric cells at 10 mA cm^{-2} and set capacity of 1 mAh cm^{-2}, and (b) the Zn@TiO_2/NC||Zn@TiO_2/NC cell at 10 mA cm^{-2} and set capacity of 5 mAh cm^{-2}.

The two symmetric cells using bare Zn and Zn@TiO_2/NC, respectively, were tested by recording the dependence of voltage on time while applying a constant current for electrodeposition. Fig. S21a-c show the voltage-time profiles of the two symmetric cells when applied constant current at 1, 2, and 5 mA cm^{-2}, respectively. Apparently, the peak current of Zn@TiO_2/NC is smaller than that of the bare Zn. Comparisons of their peak current values at 1, 2, and 5 mA cm^{-2}, respectively, are shown in Fig. S21d.

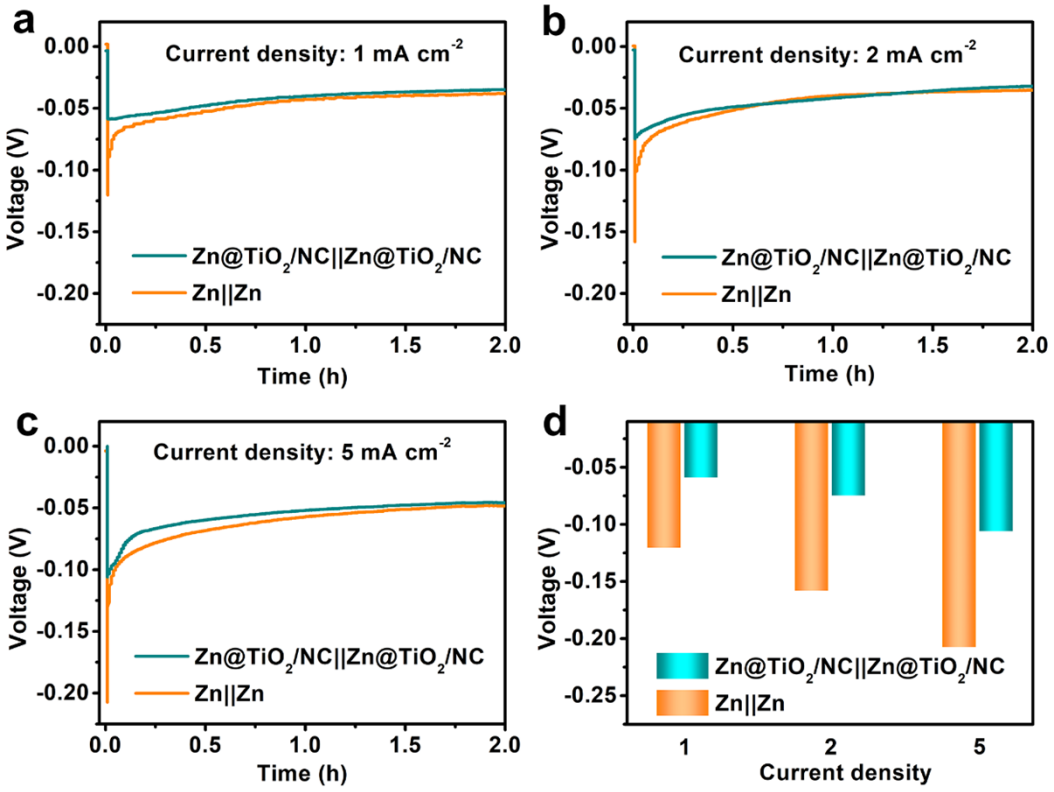

Fig. S21 Voltage-time plots showing galvanostatic nucleation overpotentials of a Zn||Zn cell and a Zn@TiO_2/NC||Zn@TiO_2/NC cell tested at current densities of (a) 1, (b) 2, and (c) 5 mA cm^{-2}. (d) Comparisons of peak potentials between the two cells.

Fig. S22 shows FESEM images of a bare Zn anode after being cycled at 5 mA cm^{-2} for 60 h. I can be seen that this Zn electrode was suffered from severe dendrite growth.

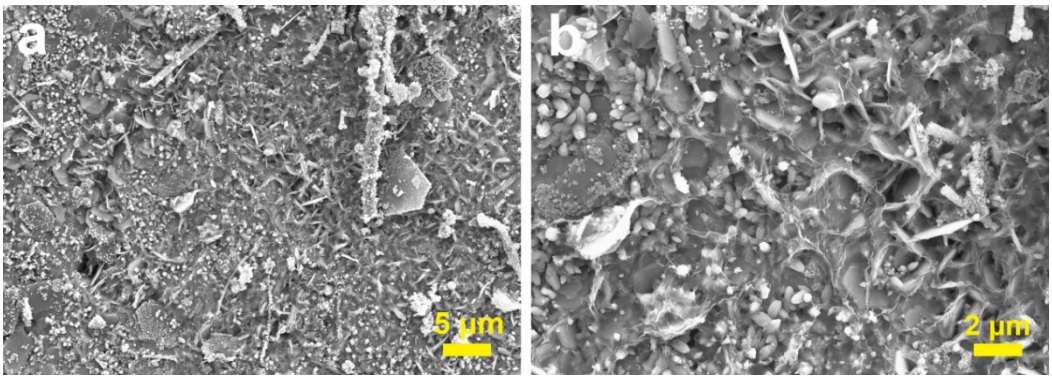

Fig. S22 (a) low- and (b) high-magnification FESEM images showing the surface morphologies of the bare Zn after being cycled at 5 mA cm^{-2} and set capacity of 1 mAh cm^{-2} for 60 h.

The surface morphologies of Zn@TiO_2 and Zn@NC after being cycled in symmetric cells are shown in Fig. S23.

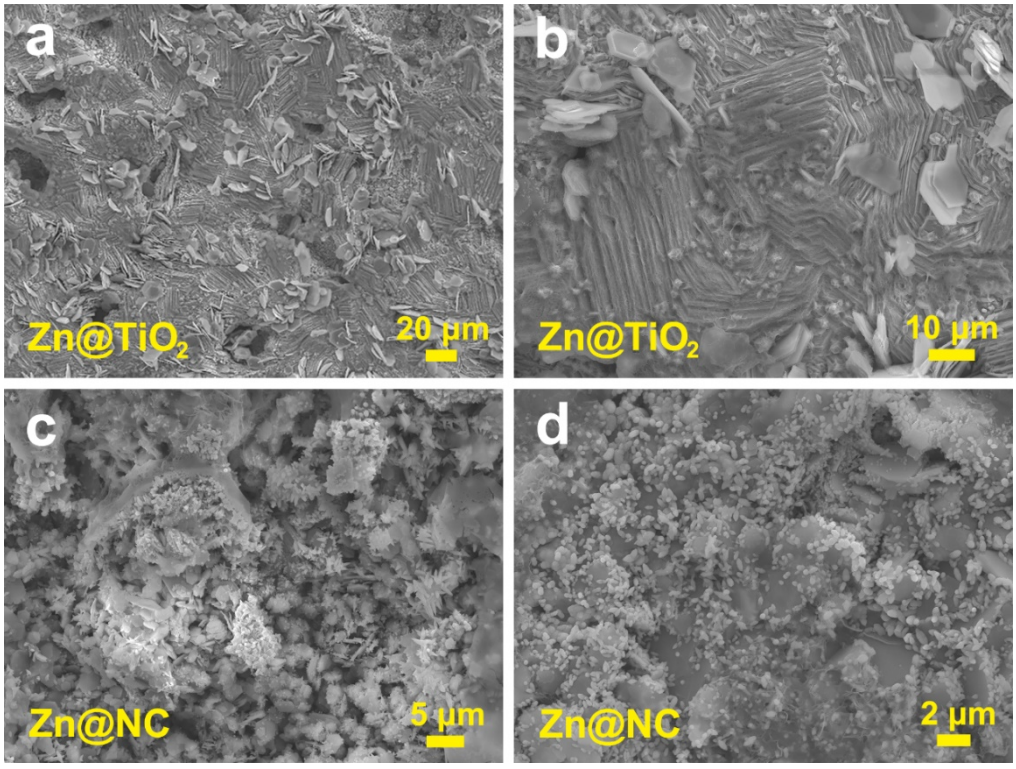

Fig. S23 FESEM images showing surface morphologies of (a, b) the Zn@TiO_2 and (c,

d) the Zn@NC in symmetric cells after the cycling test.

Characterizations of α-MnO_2 cathode material

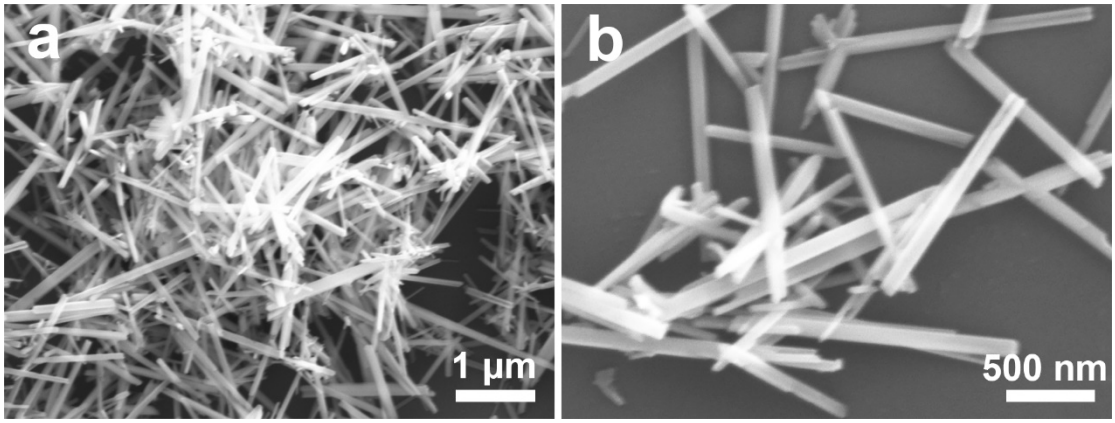

Fig. S24 FESEM images of as-prepared α-MnO_2 nanorods at (a) low and (b) high magnifications.

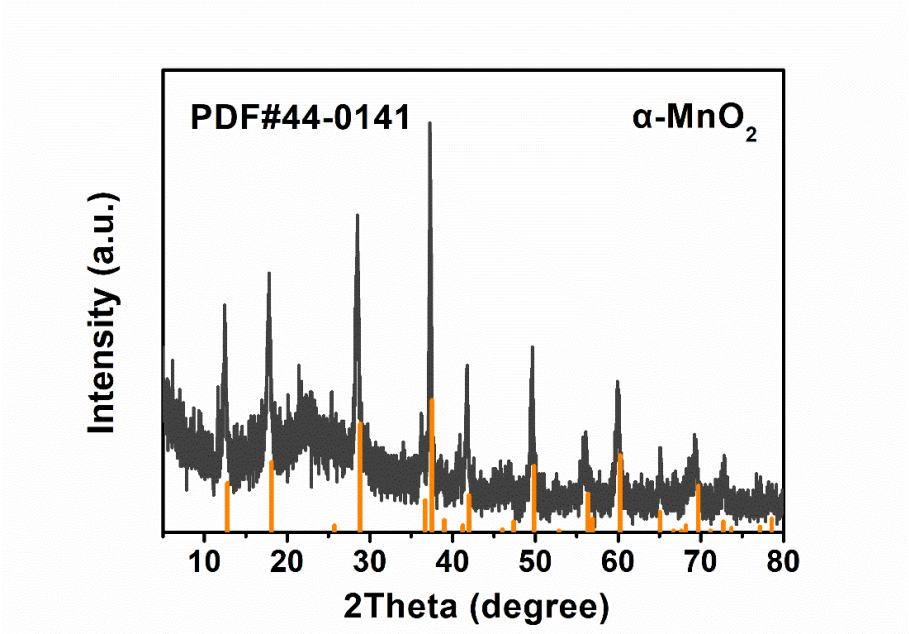

Fig. S25 XRD pattern of the α-MnO_2 nanorods.

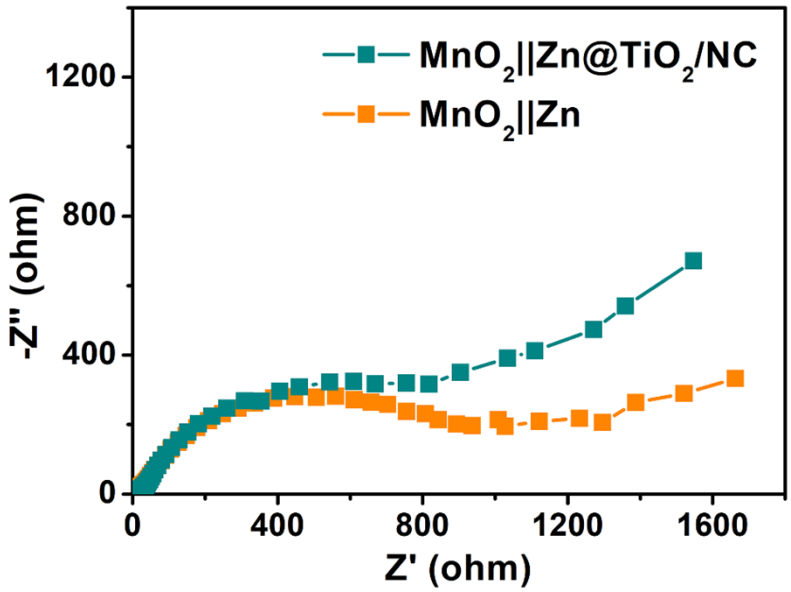

Fig. S26 Nyquist plots of the MnO_2-based full cells with bare Zn and Zn@TiO_2/NC anodes, respectively.

Table S1 The charge-transfer resistance (Ω) of the symmetrical cells with bare Zn and the Zn-TiO_2@NC anode at various temperatures.

Temperature (ºC)	Zn (Ω)	Zn-TiO_2@NC (Ω)
25	1380	171
40	692	130
50	455	108
60	313	94
70	198	81
80	149	69

Table S2 Comparison of cycling performance for our work with recently reported anodes in symmetric cells.

Electrode	Current density (mA cm^{-2})	Areal capacity (mAh cm^{-2})	Voltage hysteresis (mV)	Life (h)	Ref.
100TiO_2@Zn	1	1	57.2	150	41
MOF-coated Zn	3	0.5	80	500	12
MXene@Zn	1	1	41.5	300	42
PAM-Zn	2	4	46.5	280	13
MOF-based Zn	1	1	20	400	20
Zn-Graphite	0.1	0.1	28	200	43
ZnS@Zn	2	2	≈50	1100	25
SEI-Zn	5	1	50	220	34
Zn|In	1	1	≈120	510	27
Zn@ZIF	2	2	30	700	22
100Al_2O_3@Zn	1	1	≈50	500	26
502 glue-coated Zn	2	1	≈55	400	28
Zn-TiO_2@NC	**5**	**1**	**50**	**1100**	**This**
	2	**1**	**20**	**750**	**work**

[S1] VandeVondele, J.; Hutter, J. Gaussian basis sets for accurate calculations on molecular systems in gas and condensed phases. *Comput. Phys. Commun.* **2007**, 127 (11), 114105.

[S2] Grimme, S. FESEMiempirical Gga-Type Density Functional Constructed with a Long-Range Dispersion Correction. *J. Comput. Chem.* **2006**, 27, 1787.

[S3] Perdew, J. P.; Burke, K.; Ernzerhof, M. Generalized Gradient Approximation Made Simple. *Phys. Rev. Lett.* **1996**, 77 (18), 3865-3868.

[S4] Lippert, B. G.; Parrinello, J. H.; Michele, A hybrid Gaussian and plane wave density functional scheme. *Mol. Phys.* **1997**, 92 (3), 477-488.

[S5] VandeVondele, J.; Hutter, J. Gaussian basis sets for accurate calculations on molecular systems in gas and condensed phases. *J. Chem, phys.* **2007**, 127 (11), 114105.

[S6] Goedecker, S.; Teter, M.; Hutter, J. Separable dual-space Gaussian pseudopotentials. *Phys. Rev. B* **1996**, 54 (3), 1703-1710.